Two-photon inner-shell transitions in xenon atoms

Ilakovac, Ksenofont; Tudorić-Ghemo, J.; Kaučić, S.

Two-photon inner-shell transitions in xenon atoms

K. Ilakovac
Department of Physics, Faculty of Science, University of Zagreb, P.O. Box 162, 41001 Zagreb, Croatia, Yugoslavia and R. Bošković Institute, P.O. Box 1016, 41001 Zagreb, Croatia, Yugoslavia

J. Tudorić-Ghemo
Faculty of Electrical and Mechanical Engineering and Naval Architecture, Ul. R. Boškovića, 58000 Split, Croatia, Yugoslavia

S. Kaučić
R. Bošković Institute, P.O. Box 1016, 41001 Zagreb, Croatia, Yugoslavia
(Received 3 May 1991)

Decay of single-K-shell-vacancy states of xenon atoms by the emission of photon pairs that continuously share the transition energy was studied. The vacancy states were generated by electron-capture decay in ^{131}Cs. A pair of high-purity germanium detectors and a fast-slow coincidence system with a $(128\times512\times512)$-channel pulse-height analyzer were used in the measurements. Accurate energy calibration was made by a careful determination of positions of peaks due to crosstalk among the detectors via Ge K x rays. Identification of events due to the two-photon decay is based on the shifts of energy sums. From the numbers of events in the ridges, the relative differential probabilities of $2s\rightarrow1s$, $3s\rightarrow1s$, $3d\rightarrow1s$, and $4sd\rightarrow1s$ two-photon decay were derived. They are compared to the values derived from the results of non-relativistic calculations for hydrogen and hydrogenic ions of Shapiro and Breit [Phys. Rev. **113**, 179 (1959)], of Tung, Ye, Salamo, and Chan [Phys. Rev. A **30**, 1175 (1984)], and of Florescu [Phys. Rev. A **30**, 2441 (1984)], and to the results of the following studies of two-photon decay of single-K-shell-vacancy states of xenon atoms: a calculation based on the theory of Bannett and Freund [Phys. Rev. Lett. **49**, 539 (1982); Phys. Rev. A **30**, 299 (1984)], a nonrelativistic calculation of Wu and Li [J. Phys. B **21**, 1509 (1988)], and relativistic calculations of Mu and Crasemann [Phys. Rev. Lett. **57**, 3039 (1986); Phys. Rev. A **38**, 4585 (1988)], and of Tong, Li, Kissel, and Pratt [Phys. Rev. A **42**, 1442 (1990)]. As expected, no events due to the $np\rightarrow1s$ two-photon transitions were observed and upper limits are given.

PACS number(s): 31.30.Jv, 32.30.Rj, 32.80.Wr

INTRODUCTION

The process of emission of photon pairs that continuously share the transition energy is closely related in two atomic systems: hydrogenic systems and many-electron systems with a single inner-shell vacancy. In many systems single-particle and single-hole states have many common features. The decay of an inner-shell vacancy state may be visualized to proceed via essentially the same states (with regard to the quantum numbers) as in the case of a hydrogenic system, but in the opposite order. The wave functions and energies of the states are, of course, different. In one aspect the two systems show a major difference. In the hydrogenic systems, the metastable $2s$ state occurs, which cannot decay by the fast electric dipole ($E1$) transition. No metastable inner-shell-vacancy states exist in many-electron systems, because in higher shells electrons satisfying the $E1$ selection rule ($\Delta l=\pm1$) are always available.

Decay of the metastable $2s$ state of hydrogen by the emission of a pair of photons was first considered by M. Göppert-Mayer in 1931 [1]. Further studies [2] have shown that the emission of two electric dipole photons ($E1$-$E1$ transition) is the main mechanism of decay of the metastable $2s$ state. The second-order perturbation theory and nonrelativistic electric dipole approximation was also applied by Shapiro and Breit [3] in their extensive calculations of the transition matrix elements involving bound (discrete) and unbound intermediate np states. They obtained a very reliable result on the transition probability of $E1$-$E1$ decay of the metastable $2s$ state in hydrogenic systems of atomic number Z, $1/\tau=8.226Z^6\ \mathrm{s}^{-1}$. Several subsequent calculations were performed using also the nonrelativistic electric dipole approximation. Zon and Rapoport [4] derived a simple analytic expression for the differential transition probabilities of $2s\rightarrow1s$ decay which avoids cumbersome (and approximate) summation of infinite series. Klarsfeld [5] derived a modified expression and calculated a rather accurate result for the total transition probability in this approximation, $1/\tau=(8.2282\pm0.0001)Z^2\ \mathrm{s}^{-1}$. With the new values of the fundamental physical constants [6] we obtain from both the Zon and Rapoport and the Klarsfeld expressions the total transition probability of $2s\rightarrow1s$ decay $1/\tau=Z^6 8.229\,355\ \mathrm{s}^{-1}$, accurate to 6 ppm. Tung, Ye, Salamo, and Chan [7] calculated the differential transition probabilities between any pair of states $(n_1,l_1,m_1)\rightarrow(n_2,l_2,m_2)$ of a hydrogenic system that

satisfy the electric dipole selection rule. Florescu [8] applied a different approach to calculate the $3s \rightarrow 1s$ and $3d \rightarrow 1s$ differential transition probabilities. Costescu, Brândus, and Mezinescu [9] derived general analytic expressions for the differential transition probabilities between any pair of states which, according to their checks, reproduce the results of Tung, Ye, Salamo, and Chan [7] and of Florescu [8].

Very elaborate relativistic calculations [10,11] of transition probabilities for $2s \rightarrow 1s$ decay by emission of photon pairs in hydrogenic systems show that $1/(Z^6\tau)$ is not a constant as in the nonrelativistic electric dipole approximation, but a decreasing function of Z.

Experimental investigation of the process of emission of photon pairs from hydrogenic systems in the $2s$ state is rather difficult. A broad peak observed in the spectrum emitted from a neon plasma was interpreted as due to the $2s \rightarrow 1s$ double-photon decay in Ne^{9+} ions [12]. Hinds, Clendenin, and Novick [13] made elaborate and precise measurements of decay of the metastable $2s$ state in He^+ ions by observing decay in flight of the ions in a drift tube by means of a movable detector. The beam-foil technique of production of fast, highly ionized heavy ions allowed accurate measurements of decay of the metastable states in several hydrogenic and heliumlike systems [14,15], which provide accurate tests of the calculated decay rates. A precise measurement [16] of the decay rate of the metastable $2\,^1S_0$ state in He-like krypton has shown a departure from the nonrelativistic theory. Mean life of the state was found to be longer by about 6.7%, in accord with the result of relativistic calculations.

Freund [17] initiated the study of emission of photon pairs from many-electron systems with an inner-shell vacancy. He made approximate calculations of such two-photon decay of a K-shell vacancy in copper atoms using second-order perturbation theory and relating the relevant matrix elements to the absorption cross sections and oscillator strengths. Unoccupied bound and unbound states were assumed in the sum over intermediate states. Bannett and Freund [18] measured the two-photon decay in molybdenum atoms irradiated by a beam of silver K x rays. They used a pair of Si(Li) detectors, and a coincidence system with three-parameter recording of data. From the experimental data they derived the absolute values of matrix elements of two-photon decay. They also developed a calculation using a second-order perturbation theory and nonrelativistic electric dipole approximation, Roothaan-type wave functions, and frozen orbitals. The sum over intermediate states was carried out over unoccupied as well as occupied bound states and over unbound states. For $2s \rightarrow 1s$ decay they obtained good agreement with the experimental results. They also reported higher-shell $\rightarrow 1s$ results with an intensity about twice the intensity of $2s \rightarrow 1s$ decay. Ilakovac *et al.* [19] reported the results on $2s \rightarrow 1s$, $3s \rightarrow 1s$, $3d \rightarrow 1s$, and $4sd \rightarrow 1s$ two-photon decay in xenon atoms, elaborated in more detail in the present report. Mu and Crasemann [20] made a detailed calculation of two-photon decay in xenon atoms, which was later extended also to the decay of molybdenum and silver atoms [21]. They used second-order perturbation theory and also Dirac-Hartree-Slater wave functions calculated in the self-consistent-field potential assuming a single-K-shell vacancy. Many multipoles of the radiation field were taken, and summation over intermediate states was performed over occupied and unoccupied bound states and over the states in continuum.

Assuming the single-particle model but taking into account many-body interaction effects, Guo [22] gave a fundamental proof that the Pauli principle does not prohibit summation over occupied bound states, as has already been assumed in earlier work [18,20].

Wu and Li [23] made a nonrelativistic self-consistent-field calculation, using the electric dipole approximation, of the relative differential transition probabilities of two-photon decay in argon, krypton, xenon, and radon. Tong, Li, Kissel, and Pratt [24] extended the study by making an elaborate relativistic self-consistent-field calculation of two-photon decay taking many multipoles into account. From the comparison with the nonrelativistic results [23], Tong, Li, Kissel, and Pratt [24] conclude (i) that the screening due to electrons in many-electron systems treated in nonrelativistic self-consistent-field electric dipole approximation reduces the transition probabilities in comparison to the nonrelativistic results for hydrogenic systems (the effect increases at larger Z), and (ii) that relativistic effects cause a further reduction (but the effect becomes relatively smaller at larger Z). The results of Mu and Crasemann [21] show a good agreement with the results of Tong, Li, Kissel, and Pratt [24] for $ns \rightarrow 1s$ two-photon decay, but are some 36% smaller for $nd \rightarrow 1s$ two-photon decay.

In this paper a detailed report is given on measurements, analysis, and results of a study of two-photon decay in xenon atoms, reported earlier [19]. Two corrections have been introduced: a factor of 0.5 was omitted in the calculation of the relative differential probabilities and the treatment of the background was improved by taking into account events due to crosstalk among the detectors via germanium $K\alpha$ and $K\beta$ x rays accompanied by the absorption of xenon L x rays in the detectors. Several calculations of two-photon decay in xenon atoms (as reported above) have recently been made that allow detailed comparison among them and with the experimental results.

MEASUREMENTS

Radioactive ^{131}Cs was produced in the nuclear reactor of the Boris Kidrič Institute (near Belgrade), by the irradiation of 3 g of $BaCO_3$, sealed in a quartz ampoule, in a flux of about 3.5×10^{13} neutrons/(cm^2s) for 135 h. Radiochemical separation and purification of ^{131}Cs was made by the following operations. Cesium was removed from the irradiated sample by triple recrystallization of $BaCl_2$. The purified $BaCl_2$ was introduced into a column filled with the Bio-Rad cation exchange resin Dowex 50 WX^+, 100–200 mesh. After 14 days, when the maximum radioactivity of ^{131}Cs was expected, elution of cesium with $1N$ HCl was made. Finally, the solution was introduced into a smaller Bio-Rad cation exchange column, followed by elution with $0.5N$ HCl. The last operation was repeated once. The initial radioactivity of the

prepared ^{131}Cs source was about 46 MBq. Its radioactive purity was checked using a Ge (Li) γ-ray spectrometer. Weak contamination by ^{131}Ba, ^{134}Cs, ^{59}Fe, and ^{60}Co was found, their radioactivity being almost eight orders of magnitude less than that of ^{131}Cs.

In the course of the measurements ten weak sources were used. Their initial activities were between 0.9 and 1.2 kBq. Each of the sources was prepared by putting a small droplet of the $^{131}CsCl_2$ solution on a polyethylene sheet, into which a small piece of pure cellulose paper (about 0.4-mm diam) was placed. After drying, the small radioactive piece of paper was placed between two 0.06-mm-thick foils of polyethylene and carefully centered in the hole of the shield. The shield was made of aluminum, its thickness was 2.6 mm, the hole in the shield was of a double-conical form, and the opening (where the source was centered) had a diameter of about 0.7 mm.

The shield with the source was placed between two high-purity (HP) germanium planar detectors (supplied by Ortec, Oak Ridge) of a nominal size 200 mm^2×7 mm thick, in a close 180° geometry (Fig. 1). The short-term energy resolution of the detectors at 5.9 keV was about 230 to 240 eV, and the long-term resolution at about 30 keV, determined from the complete set of the three-parameter data, was about 375 eV. The time resolution of the system for pairs of photons of energy above 10 keV was about 20 ns.

The fast-slow coincidence system with the three-parameter [(128×512×512)-channel] pulse-height analyzer (Fig. 2) recorded the time difference (k_0 channel) and the amplitudes (k_1 and k_2 channel numbers) of pulse pairs arriving from the two detectors within the time resolution of the coincidence unit ($2\tau \approx 250$ ns). Prior to the start and after each measurement careful calibration and checks of the apparatus were made.

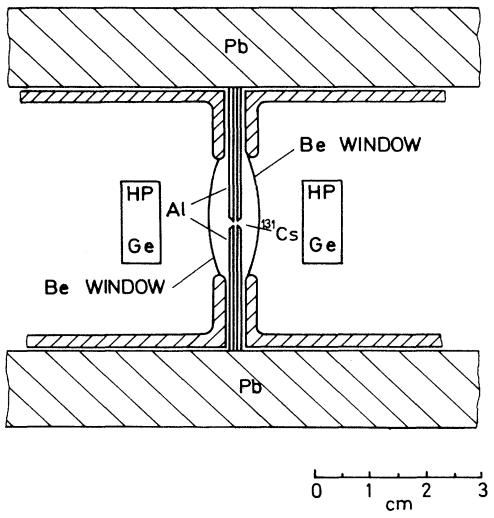

FIG. 1. Experimental arrangement. Actual distance of the front surfaces of the high-purity germanium (HP Ge) detectors from the source was smaller (8.0 mm) than shown in the figure.

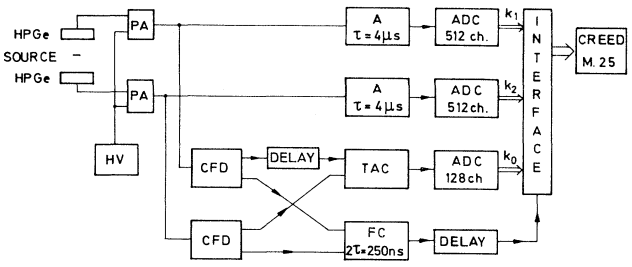

FIG. 2. Block diagram of electronics. High-purity germanium detectors (HP Ge) were fed by a high-voltage unit (HV). Pulses from the preamplifiers (PA's) were branched into amplifiers (A) and constant-fraction discriminators (CFD's). Amplified pulses were analyzed in 512-channel analog-to-digital converters (ADC's). Fast (negative) pulses from the CFD's were used as start and stop (after delay by about 100 ns) signals for the time-to-amplitude converter (TAC). Its output was analyzed in a 128-channel ADC. Positive pulses from the CFD's were led into the coincidence unit ($2\tau \approx 250$ ns) which activated the interface unit to make the record of outputs from all three ADC's in a paper-tape perforator (CREED model 25).

ANALYSIS OF DATA

Ten records of three-dimensional data made in the course of the measurements were checked for consistency by comparing the positions of characteristic peaks in one-dimensional spectra which were made by projecting the three-dimensional data of each record onto the k_0 (time), k_1, and k_2 (energy) axes. Nine records were found to differ in peak positions by one channel or less and have been treated as one set of data. Total collection time for the nine records was 1757 h. The record of one measurement was rejected.

A projection of the three-dimensional data in the direction of the k_0 axis (i.e., onto the k_1-k_2 plane) for an in-coincidence interval of k_0 channels, yields a table of numbers of events, the E_1-E_2 (two-dimensional) energy spectrum. A schematic representation of the E_1-E_2 spectrum for the present measurement is shown in Fig. 3. The E_1-E_2 spectrum displays several distinct peaks in the analyzed region. In Fig. 3 they are represented by circles. Some of the peaks overlap. The peaks are due to the crosstalk among the detectors by the exchange of Ge $K\alpha$ and Ge $K\beta$ x rays [25]. In the absorption of a xenon K x ray in the sensitive volume of one HP Ge detector a K electron may be ejected from a germanium atom, giving rise to the emission of a $K\alpha$ or $K\beta$ x ray. The germanium K x rays may escape from the sensitive volume of the detector, pass through the small hole in the shield, and be absorbed in the other HP detector. Such processes give rise to the real coincidence events in which an energy E(Xe K x)-E(Ge K x) is deposited in one detector and an energy E(Ge K x) in the other. We denote them as (Xe K x-Ge K x)−Ge K x events. In addition to the strong (Xe K x-Ge K x)−Ge K x peaks (numbered 1–8 in Fig. 3 and Table I) another set of very weak peaks (num-

bered 9–16) was to be expected. These peaks will presently be discussed. The (Xe K x-Ge K x)–Ge K x peaks were very useful in the analysis of timing and allowed a very accurate energy calibration. Analysis of timing was made by making projections of the three-parameter data onto the k_0 axis for many sections of the E_1-E_2 spectrum. For an illustration the time spectra for sections (B), (C), and (D) of Fig. 3 are shown in Fig. 4. The time per channel, determined by inserting a 10-m-long coaxial cable either in the start or in the stop input of the time-to-amplitude converter, was about 2.6 ns/channel. The full width at half maximum (FWHM) of the time resolution was about 20 ns.

The close agreement among the time spectra shown in

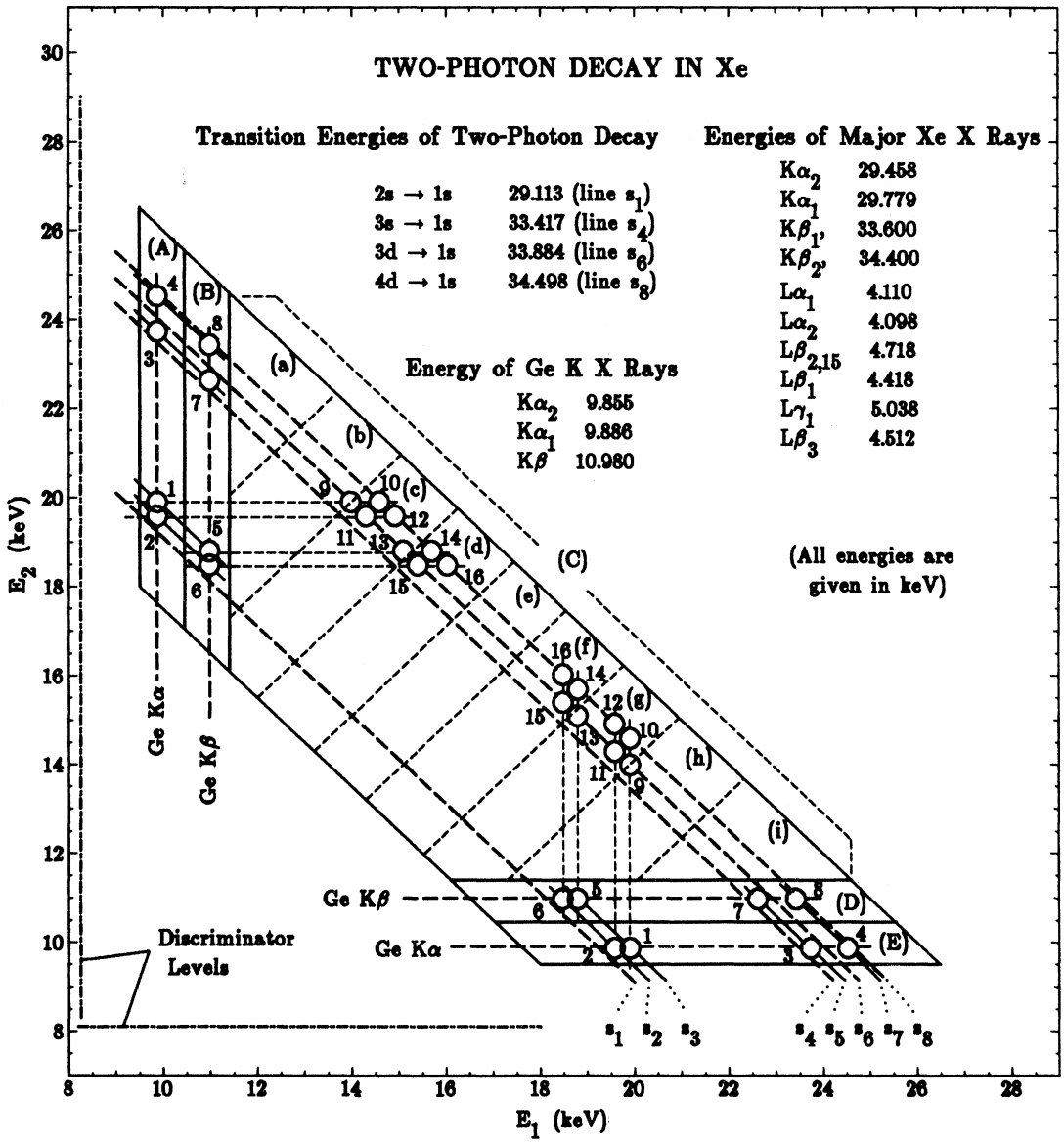

FIG. 3. Schematic representation of the two-dimensional E_1-E_2 spectrum drawn to scale. The circles represent the two-dimensional peaks. The diameter of the circles represents the full-width-at-half-maximum (FWHM) energy resolution of the detectors. The two-dimensional peaks numbered 1–8 are due to crosstalk among the detectors via Ge K x rays (see the text and Table I). They lay on constant sum-energy lines denoted by s_2, s_3, s_5, and s_7 corresponding to the energy of $K\alpha_2$, $K\alpha_1$, $K\beta_1$, and $K\beta_2$ x-ray transitions in xenon. The dashed lines at constant sum energy denoted by s_1, s_4, s_6, and s_8 show the positions of ridges due to $2s \rightarrow 1s$, $3s \rightarrow 1s$, $3d \rightarrow 1s$, and $4sd \rightarrow 1s$ two-photon decay, respectively. The crosstalk events accompanied by absorption of L x rays of xenon also lay on the constant sum-energy lines s_1, s_4, s_6, and s_8. Sections (A), (B), (D), and (E) of the E_1-E_2 spectrum, containing the peaks due to (Xe K x)-Ge K x)–Ge K x events, were analyzed to determine the timing, the energy scales, and the energy resolution. Section (C) and its subsections (a), (b), . . . , (i) were analyzed to determine the numbers of events due to the two-photon decay.

Fig. 4 is an assurance that the time shifts in the central (C) section of the E_1-E_2 spectrum are negligible. The time spectra for sections (A) and (E) of Fig. 3 (not shown) have visible shifts, and for sections still closer to the discriminator thresholds the shifts become considerable and the shape of the peaks changes. For that reason the results in Ref. [19] on $3s \rightarrow 1s$, $3d \rightarrow 1s$, and $4sd \rightarrow 1s$ two-photon decay at an energy of one photon of 8.4 keV are considered unreliable. In the present analysis only data in section C were used to derive the transition probabilities of two-photon decay.

On the basis of the analysis of time spectra a new E_1-E_2 spectrum was made with the following intervals of time channels: $k_0=37-61$ for the region above the discriminator threshold in branch 1 and for section (A), $k_0=51-64$ for section (B), $k_0=51-65$ for section (C), $k_0=52-64$ for section (D), and $k_0=53-70$ for the region above the discriminator threshold in branch 2 and for section (E). The new E_1-E_2 two-dimensional spectrum was the basis of all subsequent analyses.

The energy scales on the k_1 and k_2 axes were determined very carefully because spectra of closely-spaced peaks had to be analyzed. The two-dimensional (Xe K x-Ge K x)–Ge K x crosstalk peaks allowed accurate determination of six energy points on the k_1 axis, six energy points on the k_2 axis, and two energy points on the k_1+k_2 (sum-spectrum) axis. The six energy points on the k_1 (or k_2) axis were the positions of the peaks numbered 1, 3, 5, and 7 in Table I. The six energies were 9876, 10 980, 19 903, 23 724, 18 799, and 22 620 eV. Two energy points on the k_1+k_2 axis corresponded to the energy of Xe $K\alpha_1$ (29 779 eV) and Xe $K\beta_1$ (33 600 eV) x rays. The sum spectrum of each of the sections (A), (B), (D), and (E) shown in Fig. 3 yielded one pair of sum-energy points.

Positions of the peaks were determined in three ways: (i) sections around the peaks were projected onto the k_1 and k_2 axes and the one-dimensional spectra were analyzed, (ii) sections around the peaks were projected onto the k_1+k_2 axis and one-dimensional spectra were analyzed, and (iii) sections (A), (B), (D), and (E) were analyzed as two-dimensional spectra and a surface-fitting routine was applied. In the one-dimensional spectra each peak was represented by an over-channel-integrated Gaussian function and by a "low-energy shoulder," an integral Gaussian function. Central points and variances of the two functions were assumed to be the same. In addition to the positions of two peaks, variable parameters were three peak amplitudes (the ratio of numbers of events in the peaks due to the $K\alpha_2$ and $K\alpha_1$ x rays was assumed equal to 0.551, the corrected value of 0.539 for detection efficiency of crosstalk events), zero-energy variance [it was assumed $\sigma^2(E)=\sigma_0^2+FE_0E$, where $\sigma^2(E)$ is the variance at photon energy E, σ_0^2 the variance at $E=0$, $F=0.08$ the Fano factor, and $E_0=2.95$ eV the energy per electron-hole pair in germanium], relative height of the "low-energy shoulder" of peaks, and a constant background. The two-dimensional spectra were represented by two-dimensional peaks (two-dimensional Gaussian functions integrated over squared channels). In addition to the peak positions and amplitudes, variable parameters were the peak widths in either dimension and

TABLE I. Peaks in the E_1-E_2 spectrum due to crosstalk. The absorption of a Xe K x ray and the escape of a Ge K x ray from the sensitive volume of one detector, and a simultaneous absorption of the escaped Ge K x ray in the other detector is denoted as (Xe K x-Ge K x)–Ge K x coincidence event. If this event is accompanied by a simultaneous absorption of a Xe L x ray in the other detector it is denoted as (Xe K x-Ge K x)–(Ge K x+Xe L x) coincidence event. Each peak in this table appears as a pair of peaks in the E_1-E_2 spectrum because of symmetry of the experimental system on exchange of the detectors (see Fig. 3).

Peak number (Fig. 3)	Event in one detector	Energy (eV)	Event in the other detector	Energy (eV)
1	Xe $K\alpha_1$-Ge $K\alpha$	19 903	Ge $K\alpha$	9 876
2	Xe $K\alpha_2$-Ge $K\alpha$	19 583	Ge $K\alpha$	9 876
3	Xe $K\beta_1$-Ge $K\alpha$	23 724	Ge $K\alpha$	9 876
4	Xe $K\beta_2$-Ge $K\alpha$	24 524	Ge $K\alpha$	9 876
5	Xe $K\alpha_1$-Ge $K\beta$	18 799	Ge $K\beta$	10 980
6	Xe $K\alpha_2$-Ge $K\beta$	18 478	Ge $K\beta$	10 980
7	Xe $K\beta_1$-Ge $K\beta$	22 620	Ge $K\beta$	10 980
8	Xe $K\beta_2$-Ge $K\beta$	23 420	Ge $K\beta$	10 980
9	Xe $K\alpha_1$-Ge $K\alpha$	19 903	Ge $K\alpha$+Xe $L\alpha$	13 985
10	Xe $K\alpha_1$-Ge $K\alpha$	19 903	Ge $K\alpha$+Xe $L\beta_{2,15}$	14 594
11	Xe $K\alpha_2$-Ge $K\alpha$	19 583	Ge $K\alpha$+Xe $L\beta_1$	4 294
12	Xe $K\alpha_2$-Ge $K\alpha$	19 583	Ge $K\alpha$+Xe $L\gamma_1$	14 914
13	Xe $K\alpha_1$-Ge $K\beta$	18 799	Ge $K\beta$+Xe $L\alpha$	15 089
14	Xe $K\alpha_1$-Ge $K\beta$	18 799	Ge $K\beta$+Xe $L\beta_{2,15}$	15 698
15	Xe $K\alpha_2$-Ge $K\beta$	18 479	Ge $K\beta$+Xe $L\beta_1$	15 398
16	Xe $K\alpha_2$-Ge $K\beta$	18 479	Ge $K\beta$+Xe $L\gamma_1$	16 018

a constant background. The three methods of analysis yielded highly consistent results. The correlation coefficient of linear fits of the energy scales on either axis deviated from 1 by less than 10^{-7}. On the basis of the above analysis we consider the derived energy scales on the k_1 and k_2 axes accurate to about 5 eV in the energy range 9–24 keV, and the energy scale on the k_1+k_2 axis accurate to about 8 eV in the energy range 29–35 keV. Fitting of the four sum spectra derived from sections (A), (B), (D), and (E) (shown in Fig. 3) yielded four values of σ_0. In the analysis of data due to two-photon decay the average value of the four values of σ_0 was assumed.

Identification of the events due to two-photon decay was based on energy considerations. The sum energy of the photon pair due to $2s \rightarrow 1s$ two-photon decay is lower than the sum energy of a (Xe $K\alpha_2$-Ge K x)–Ge k x crosstalk event, because the latter is due to an initial $K\alpha_2$ x ray which was emitted in a $2p_{1/2} \rightarrow 1s$ transition. The shift in the sum energy equals the difference of binding energies of $2s$ and $2p_{1/2}$ electrons. The sum energy of (Xe $K\alpha_1$-Ge K x)–Ge K x events (equal to the energy of $K\alpha_1$ x rays) is still larger because the $2p_{3/2}$ electrons have a still smaller binding energy. Similarly, sum energies of $3s \rightarrow 1s$ and $3d \rightarrow 1s$ two-photon decays are not equal to the sum energy of (Xe $K\beta_1$-Ge K x)–Ge K x events because of the different binding energies of $3s$, $3d$, and $3p$ electrons. Figures 5(a) and 5(c) show sum spectra of sections $A+B$ and of $D+E$, respectively, in which the

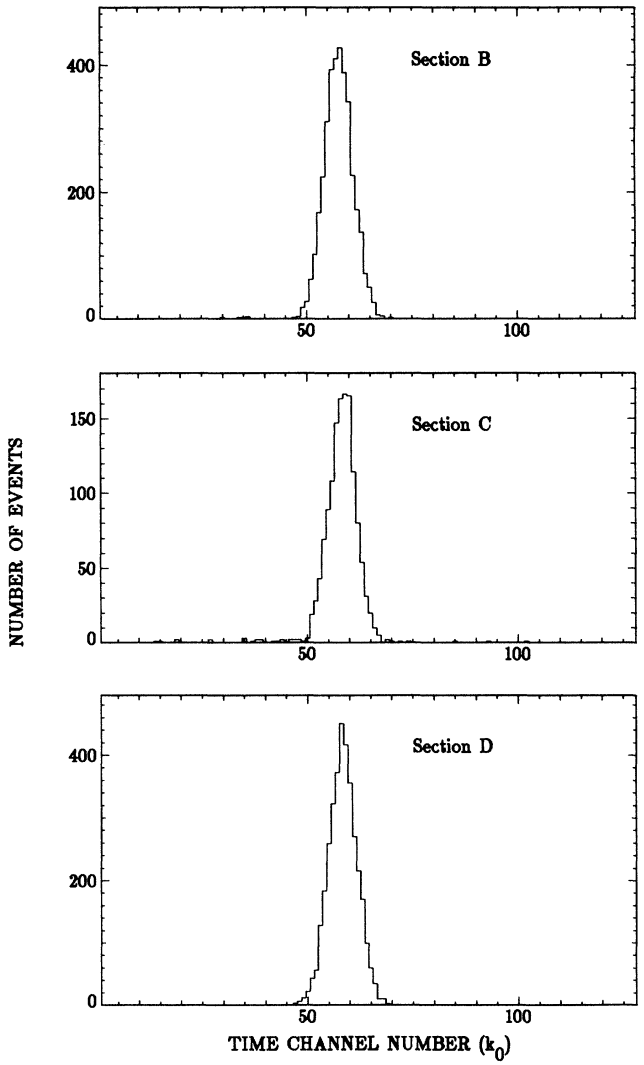

FIG. 4. Time spectra made from the three-dimensional data for sections (B), (C), and (D) shown in Fig. 3.

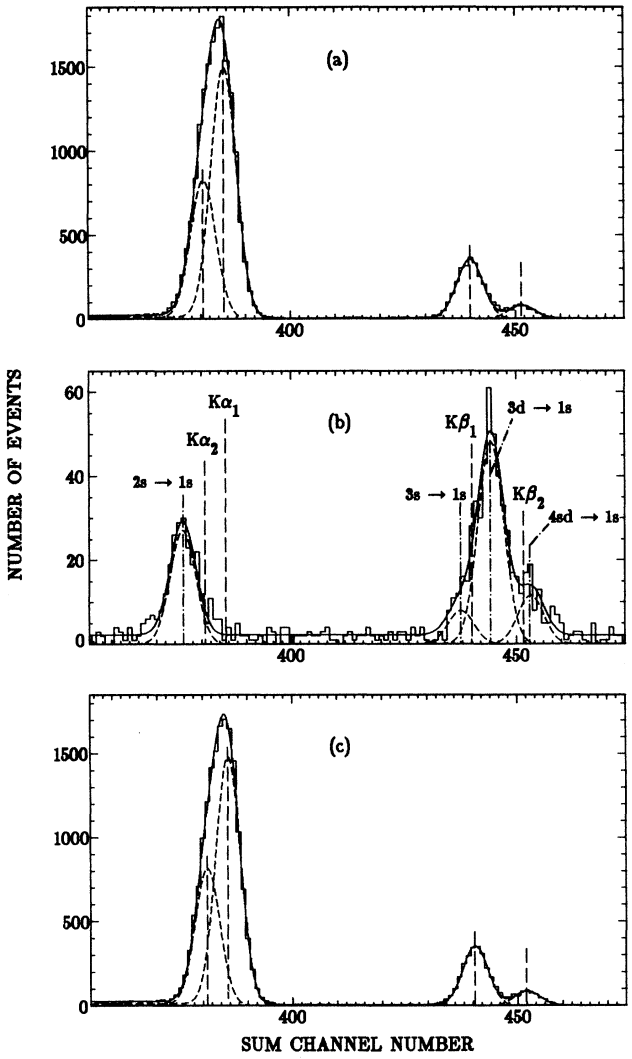

FIG. 5. Sum spectra of (a) sections (A) and (B), (b) section (C), and (c) sections (D) and (E) of the E_1-E_2 spectrum. Histograms in (a) and (c) show the peaks due to crosstalk via Ge $K\alpha$ and $K\beta$ x rays. Sum energies are equal to the energies of $K\alpha_2$, $K\alpha_1$, $K\beta_1$, and $K\beta_2$ x rays of xenon. Positions of the peaks are indicated by the dashed lines. The histogram in (b) shows shifted peaks which are due to $2s \rightarrow 1s$, $3s \rightarrow 1s$, $3d \rightarrow 1s$, and $4sd \rightarrow 1s$ two-photon decay. The expected positions of the peaks are indicated by the dash-dotted lines. The component functions of the fits are shown by the dashed curves and the total functions of the fits (which also include a constant background) are shown by the solid curves.

crosstalk events dominate. They are almost the same as the direct, ungated spectra from germanium detectors of xenon K x rays (due to the summation energy resolution is somewhat impaired and intensity ratios are modified). The spectrum in Fig. 5(b) was made by projecting the data in section (C) of the E_1-E_2 two-dimensional spectrum (but excluding the regions around the weak peaks due to crosstalk accompanied by L x-ray absorption, i.e., peaks numbered 9 to 16 in Fig. 3) onto the k_1+k_2 axis. A nonlinear curve-fitting routine (described above) was applied to analyze the three spectra. Each spectrum was assumed to have four peaks and a constant background. Shifts of peaks in Fig. 5(b) with respect to the peaks in Figs. 5(a) and 5(c) are clearly visible. The shift of the $2s \rightarrow 1s$ two-photon-decay peak in Fig. 5(b) with respect to the average value of positions of the $K\alpha_1$ peaks in Figs. 5(a) and 5(c) is equal to -671 ± 24 eV. This is in very good agreement with the expected value, the difference of binding energies of $2p_{3/2}$ and $2s$ electrons in xenon of -666 eV. Similarly, the shift of the peak due to $3d \rightarrow 1s$ two-photon decay shown in Fig. 5(b) with respect to the average value of positions of the $K\beta_1$ peaks in Figs. 5(a) and 5(c) equals 287 ± 20 eV, in very good agreement with the expected value, the difference of average values of binding energies of $3p$ and $3d$ electrons, 280 eV.

Analysis of the spectrum in Fig. 5(b) was extended assuming the presence of ridges due to continuous distributions arising from $2p_{1/2} \rightarrow 1s$ and from $2p_{3/2} \rightarrow 1s$ transitions in xenon atoms. Various processes causing a continuous splitting of energy among the detectors are possible, e.g., two-photon transitions between these states, crosstalk via bremsstrahlung caused by photoelectrons [25], etc. The analysis yielded upper limits on $2p_{1/2} \rightarrow 1s$, $2p_{3/2} \rightarrow 1s$, $3p_{1/2,3/2} \rightarrow 1s$, and $4p_{1/2,3/2} \rightarrow 1s$ two-photon decay:

$$I(2p_{1/2} \rightarrow 1s)/I(2s \rightarrow 1s) \leq 0.22 ,$$

$$I(2p_{3/2} \rightarrow 1s)/I(2s \rightarrow 1s) \leq 0.095$$

for $0.39 \leq x \leq 0.61$,

$$I(3p_{1/2,3/2} \rightarrow 1s)/I(3d_{3/2,5/2} \rightarrow 1s) \leq 0.027$$

for $0.34 \leq x \leq 0.66$, and

$$I(4p_{1/2,3/2} \rightarrow 1s)/I(3d_{3/2,5/2} \rightarrow 1s) \leq 0.26$$

for $0.33 \leq x \leq 0.67$, where $x = E/E_0$, i.e., the ratio of energy of one photon of the pair to the transition energy.

The $np \rightarrow 1s$ two-photon decay was not expected to be observed because it requires parity change. In atoms one-photon emission is dominated by electric dipole ($E1$) transitions which require $\Delta l = \pm 1$ and change of parity. Therefore emission of photon pairs is expected to be dominated by $E1$-$E1$ transitions requiring $\Delta l = 0, \pm 2$ and no parity change. An important conclusion from the analysis described above is that crosstalk causing continuous division of energy among the detectors is highly unlikely even for the very strong $K\alpha_2$ and $K\alpha_1$ x-ray lines. It may, therefore, be neglected for $K\beta_1$ and $K\beta_2$ lines. Otherwise determination of numbers of events due to $3s \rightarrow 1s$, $3d \rightarrow 1s$, and $4sd \rightarrow 1s$ two-photon decay would be much more uncertain because of the smaller energy differences.

Another process did, however, contribute to the counting of events in the ridges due to $3s \rightarrow 1s$, $3d \rightarrow 1s$, and $4sd \rightarrow 1s$ two-photon decay. In Ref. [19] it was considered but underestimated and not accounted for. A (Xe $K\alpha$-Ge K x)–Ge K x crosstalk event may be accompanied by absorption of a Xe L x ray in the same detector where the Ge K x ray was absorbed. A coincidence event occurs in which the energy E(Xe K x)-E(Ge K x) is recorded in one detector, and the energy E(Ge K x)+E(Xe L x) in the other. We designate these events by (Xe $K\alpha$-Ge K x)–(Ge K x + Xe L x). Since the emission of L x rays following the $K\alpha_1$ or $K\alpha_2$ transitions occurs by the filling of $2p_{3/2}$ or $2p_{1/2}$ vacancies, these L x-ray transitions are due to electrons originating from $3s$, $3d$, $4s$, $4d$, etc. states. Therefore the sum energies of (Xe $K\alpha$-Ge K x)–(Ge K x + Xe L x) events fit exactly the sum energies of $3s \rightarrow 1s$, $3d \rightarrow 1s$, $4sd \rightarrow 1s$ two-photon-decay events. The circles numbered 9–16 in Fig. 3 show the expected locations of the peaks due to (Xe $K\alpha$-Ge K x)–(Ge K x+Xe L x) events, and Table I lists their energies. Most intensive are the (Xe $K\alpha_1$-Ge $K\alpha$)–(Ge $K\alpha$+Xe $L\alpha$) and (Xe $K\alpha_2$-Ge $K\alpha$)–(Ge $K\alpha$+Xe $L\beta_1$) peaks. They are, however, barely visible in the E_1-E_2 spectrum (previously they were considered a statistical fluctuation). These peaks cause increased numbers of events in narrow energy ranges of photon energies at about 14.1 and 19.7 keV. The (Xe $K\alpha$-Ge $K\beta$)–(Ge $K\beta$+Xe L x) peaks are expected to be about seven times weaker because of the ratio of intensities of $K\alpha$ and $K\beta$ x rays of germanium.

A new method of analysis was devised to take into account the presence of (Xe K x-Ge K x)–(Ge K x +Xe L x) events. A linear surface fitting routine was written to represent the peaks and ridges in section (C) of the E_1-E_2 spectrum (see Fig. 3). The peaks denoted 9–16 were represented by two-dimensional Gaussian functions integrated over squared channels, of known positions and widths (as calculated from the energy calibration). Ratios of numbers of pulses in the peaks were assumed fixed at values calculated from the known intensity ratios of $K\alpha_1$ and $K\alpha_2$ x-ray lines, and of L x-ray lines of xenon [26]. So only one variable parameter, the amplitude of the (Xe $K\alpha_1$-Ge $K\alpha$)–(Ge $K\alpha$+Xe L x) peaks, was used to represent all sixteen peaks due to crosstalk accompanied by xenon L x-ray absorption. To represent the different values of amplitudes of the ridges, section (C) was divided into nine sections [denoted (a), (b, . . . , (i) in Fig. 3], and the amplitude of each ridge was assumed constant in each of the sections. All nine sections contain data on $3s \rightarrow 1s$, $3d \rightarrow 1s$, and $4sd \rightarrow 1s$ two-photon decay, but only five have data on $2s \rightarrow 1s$ two-photon decay. Therefore 32 variable parameters represented the amplitudes of data due to two-photon events. Each ridge was represented by a function that was calculated by integration of the Gaussian function from the left to the right channel limit, channel by channel. The argument of the function was the sum of the channel numbers, k_1+k_2. Also, an integral Gaussian function representing the "left shoulder" of the ridge was included. One variable parameter was

used to represent all "left shoulders," the ratio of the height of the shoulder and the corresponding peak amplitude. Positions of the ridges were calculated from the energy calibration data. One more variable parameter was used, the constant background. Equal weights were applied to obtain the results on amplitudes of peaks and ridges. The main purpose of the surface fit was to determine the numbers of pulses in the (Xe $K\alpha$-Ge K x)−(Ge K x+Xe L x) peaks. The boundaries of the nine sections were carefully selected to assure reliable results. Also fits with ten and eleven sections were made yielding similar results. The results achieved by the surface fitting were applied in the final analysis. For each of the nine sections sum spectra were made. The sum spectra were fitted by "profile functions," which were made by adding values of the component functions of the surface fit over the same channels over which the numbers of events were added when making the sum spectra. The amplitudes of the (Xe K x-Ge K x)−(Ge K x+Xe L x) peaks were fixed at values derived by the surface fit, while the variable parameters were correction factors to the amplitudes of the remaining "profile functions." A linear-fitting routine with equal weights yielded the values of the correction factors, and a linear-fitting routine with weights equal to the reciprocal numbers of events (1 for zero count [27]) yielded the errors. The correction factors deviated little from 1, i.e., the results of the surface fit to the two-dimensional spectrum of the complete section C are in good agreement with the results of curve fitting of separate sum spectra. The sum spectra of the nine sections [(a), (b), . . . , (i) in Fig. 3], the component functions of the fit, and their sum (which also

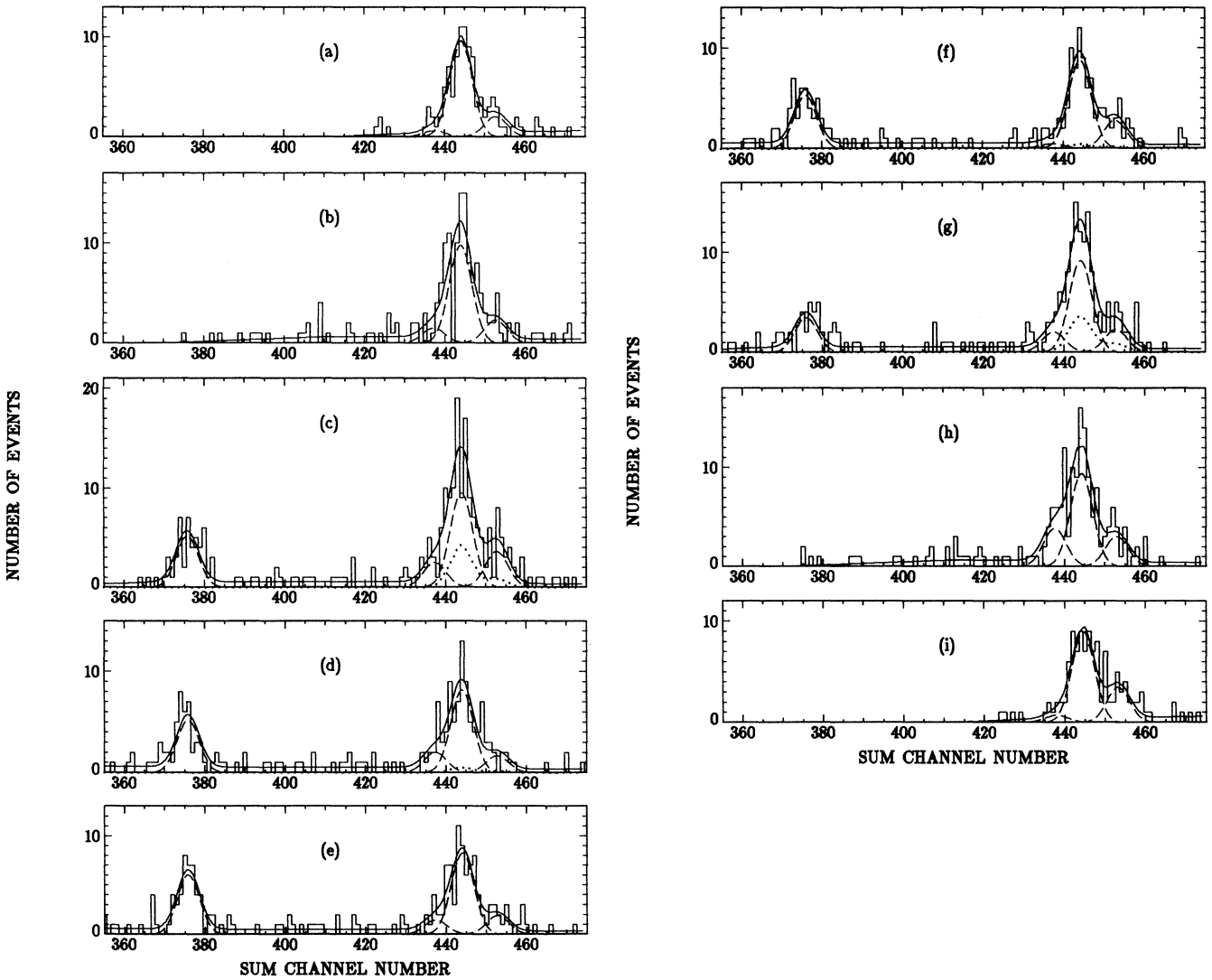

FIG. 6. Sum spectra of nine subsections of section (C) of the E_1-E_2 spectrum. They are marked (a), (b), . . . , (i) as are the corresponding sections shown in Fig. 3. Single-peak dashed curves show component functions of the fit which are due to the $2s \rightarrow 1s$, $3s \rightarrow 1s$, $3d \rightarrow 1s$, and $4sd \rightarrow 1s$ two-photon decay. The dotted curves show the component functions due to crosstalk accompanied by absorption of xenon L x rays. The upper solid curve shows the sum of the component functions and the background.

includes a constant background) are shown in Fig. 6. The results of the analysis were the numbers of counts per channel, Δn. The energy per channel was very close to $\Delta E = 70$ eV.

DERIVATION OF EXPERIMENTAL DIFFERENTIAL TRANSITION PROBABILITIES

In Ref. [19], due to a misinterpretation of normalization of the differential transition probabilities of two-photon decay, a factor of 0.5 was introduced in the expression for the calculation of the differential transition probabilities. In that paper a normalization was assumed in which the integral over solid angles of both photons and over the full energy range of one photon yields the total transition probability of two-photon decay. This is wrong because the theoretical transition probability is symmetrical on exchange of the two photons. Consider a photon pair of momenta $\mathbf{i}k_1$ and $\mathbf{j}k_2$, and a pair of momenta $\mathbf{i}k_2$ and $\mathbf{j}k_1$, where $\mathbf{i}$ and $\mathbf{j}$ are unit vectors. In the theory, because of the symmetrization, they are considered the same event. (In the experiment they are distinct events.) But when the integration over solid angles and over the full energy range is carried out, they are each counted once. For that reason the theoretical normalization is determined by

$$\int_{\Omega_1}\int_{\Omega_2}\int_0^{E_0}\frac{dW}{dE\,d\Omega_1 d\Omega_2}dE\,d\Omega_1 d\Omega_2 = 2W \ ,$$

where $dW/(dE\,d\Omega_1 d\Omega_2)$ is the differential transition probability, W the total transition probability of two-photon decay, and E_0 the transition energy. This is usually expressed by omitting the factor 2 and by integrating over energy from 0 to $E_0/2$.

The values of the relative differential transition probabilities, reported here, were derived from the expression

$$\frac{1}{W_K}\left[\frac{dW}{dE\,d\Omega_1 d\Omega_1}\right]_{\theta=\pi} = \frac{\Delta n/\Delta E}{n_K \varepsilon_1 \varepsilon_2 \varepsilon_C \Delta\Omega_1 \Delta\Omega_1 F}$$

(the previous factor of 0.5 on the right-hand side of the equation is omitted), where Δn is the number of events due to two-photon decay in an energy interval ΔE, ε_1 and ε_2 are the peak efficiencies of the detectors, ε_C is the coincidence efficiency, $\Delta\Omega_1$ and $\Delta\Omega_2$ are the solid angles of the detectors subtended from the ^{131}Cs source, and F is a correction factor. The solid angles of the detectors were $\Delta\Omega_1 = 1.61$ sr and $\Delta\Omega_2 = 1.57$ sr, the coincidence efficiency $\varepsilon_C = 0.95$, and the peak efficiencies of the detectors were $\varepsilon_1 = \varepsilon_2 = 0.95$. The correction factor F is equal to the average value over solid angles of the two detectors of the product of the angular correlation function $w(\theta)$, of the photon-attenuation factors $a(E,x)$, and of the probabilities of total energy absorption in germanium $p(E,x)$:

$$F = \langle w(\theta) a(E_1,x_1) a(E_2,x_2) p(E_1,x_1) p(E_2,x_2) \rangle \ ,$$

where $x_1 = \cos\theta_1$, $x_2 = \cos\theta_2$, and θ_1 and θ_2 are angles of photon incidence with respect to the normals to the detector surfaces (see Fig. 7). The angular correlation function was normalized to the value at $\theta = \pi$,

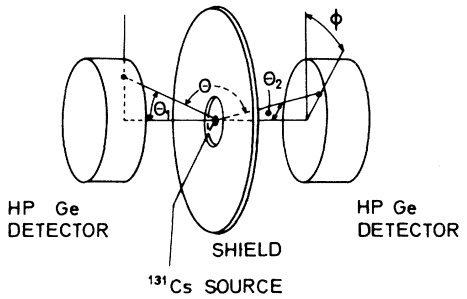

FIG. 7. Geometry for the calculation of the detection efficiency in measurements of two-photon decay.

$$w(\theta) = (1 + A_2 \cos^2\theta)/(1 + A_2) \ ,$$

with $A_2 = 1$ for $ns \rightarrow 1s$ two-photon decay, and $A_2 = \frac{1}{13}$ for $nd \rightarrow 1s$ two-photon decay. The attenuation factors take into account absorption of photons in the source, polyethylene foils, air, and beryllium windows:

$$a(E_i,x_i) = \exp(-C(E_i)/x_i) \ ,$$

$$C(E_i) = \mu_1 d_1/2 + \mu_2 d_2 + \mu_3 d_3 + \mu_4 d_4 \ ,$$

where μ_1, μ_2, μ_3, and μ_4 are photon absorption coefficients [28] for cellulose, polyethylene, air, and beryllium at energy E_i, and d_1, d_2, d_3, and d_4 are the thicknesses of the layers. The probabilities of total energy absorption of photons in germanium were calculated from the expression [25]

$$p(E_i,\theta_i) = 1 - e_1(E_i,x_i) - e_2(E_i,x_i) \ ,$$

where e_1 and e_2 are probabilities of escape of Ge $K\alpha$ and Ge $K\beta$ x rays, respectively, from germanium for photons of energy E_i incident at an angle θ_i ($x_i = \cos\theta_i$) relative to the normal to the front surface of germanium. The escape probabilities are given by

$$e_j(E_i,x_i) = \frac{1}{2}\frac{\sigma_K}{\sigma_t}\frac{w_j}{w_1 + w_2}\omega_K\left[1 - x_i r_j \ln\left[1 + \frac{1}{x_i r_j}\right]\right] \ ,$$

where σ_t and σ_K are the total and the K-shell absorption cross sections of germanium, respectively, for photons of energy E_i, w_1 and w_2 the intensity factors for the emission of $K\alpha$ and $K\beta$ x rays from germanium, ω_K the fluorescence yield, and $r_j = \mu_j/\mu(E_i)$, where μ_j, $j = 1,2$, are the absorption coefficients for Ge $K\alpha$ and Ge $K\beta$ x rays in germanium, and $\mu(E_i)$ is the absorption coefficient for photons of energy E_i in germanium. Since

$$\cos\theta = \sin\theta_1 \sin\theta_2 \cos\varphi - \cos\theta_1 \cos\theta_2$$

(see Fig. 7), assuming axial symmetry, after an integration over φ one obtains

$$F = \frac{1}{(1 - x_{1m})(1 - x_{2m})}\int_{x_{1m}}^1\int_{x_{2m}}^1 [1 + \tfrac{1}{2}a_2(1 - x_1^2 - x_2^2 + 3x_1^2x_2^2)] a(E_1,x_1) a(E_2,x_2) p(E_1,x_1) p(E_2,x_2) dx_1 dx_2 \ ,$$

TABLE II. Relative differential transition probabilities of $2s \rightarrow 1s$ two-photon decay in xenon in units of 10^{-9} keV^{-1} sr^{-2} at $\theta = 180°$. $E_0 = 29.113$ keV.

$x = E/E_0$	$\frac{1}{W_K}\frac{d^3W}{dE\, d\Omega_1 d\Omega_2}$
0.419	5.60±1.04
0.460	5.01±1.00
0.500	5.91±1.09
0.539	5.43±1.02
0.580	3.76±0.91

TABLE IV. Relative differential transition probabilities of $3d \rightarrow 1s$ two-photon decay in xenon in units of 10^{-9} keV^{-1} sr^{-2} at $\theta = 180°$. $E_0 = 33.884$ keV.

$x = E/E_0$	$\frac{1}{W_K}\frac{d^3W}{dE\, d\Omega_1 d\Omega_2}$
0.354	7.91±1.01
0.392	7.57±0.99
0.430	8.25±1.25
0.465	6.68±0.97
0.500	6.73±0.95
0.534	7.15±0.96
0.569	8.95±1.27
0.607	7.65±1.03
0.640	7.33±1.02

where $x_{1m} = \cos\theta_{1m}$ and $x_{2m} = \cos\theta_{2m}$, and θ_{1m} and θ_{2m} are the angles of incidence at which the efficiency of the detection of photons for normal incidence drops to one-half the value in the center of the detectors [29]. The values of F for pairs of values E_1, E_2 were calculated by numerical integration.

RESULTS AND DISCUSSION

Results of the analysis of experimental data are given in Tables II–V and are shown in Figs. 8–11 for $2s \rightarrow 1s$, $3s \rightarrow 1s$, $3d \rightarrow 1s$, and $4sd \rightarrow 1s$ two-photon decay in xenon atoms, respectively. For comparison the available theoretical results are also shown in the figures. The dashed curves show the theoretical results for hydrogenic xenon ions we derived from the results of nonrelativistic calculations of Shapiro and Breit [9], Tung, Ye, Salamo, and Chan [7], and of Florescu [8] (the factor of 5 for the number of electrons in $3d$ subshells was not included because a hydrogenic system is considered). Solid curves show the results for xenon atoms with a K-shell vacancy: the values calculated by our group on the basis of the theory of Bannett and Freund [18], the results of nonrelativistic self-consistent-field calculation of Wu and Li [23], and the relativistic self-consistent-field calculation of Mu and Crasemann [20,21]. The hollow squares in the figures show the results of a relativistic self-consistent-field calculation of Tong, Li, Kissel, and Pratt [24]. In all results a transition probability $W_K = 1.69 \times 10^{16}$ s^{-1} for the decay of the K-shell vacancy in xenon was assumed.

The relatively large experimental errors and a narrow energy range do not allow us to draw conclusions on the shape of the distributions. In particular the resonance effect expected for $3d \rightarrow 1s$ and $4d \rightarrow 1s$ two-photon decay was not observed. Average values of the relative differential probabilities in the central energy regions (where, because of symmetry, small variation is expected) offer better values for comparison to the theoretical results. They were calculated for 6-keV-wide intervals and are given in Table VI, together with the theoretical values of the relative differential transition probabilities of two-photon decay in xenon atoms at 180°.

Our experimental average value for $2s \rightarrow 1s$ two-photon decay is just about twice the result in Ref. [19] (due to the omission of the factor of 0.5), but for $3s \rightarrow 1s$, $3d \rightarrow 1s$, and $4sd \rightarrow 1s$ two-photon decay a factor less than 2 is found, because some counts were subtracted as background (the crosstalk events accompanied by absorption of xenon L x rays).

TABLE III. Relative differential transition probabilities of $3s \rightarrow 1s$ two-photon decay in xenon in units of 10^{-9} keV^{-1} sr^{-2} at $\theta = 180°$. $E_0 = 33.417$ keV.

$x = E/E_0$	$\frac{1}{W_K}\frac{d^3W}{dE\, d\Omega_1 d\Omega_2}$
0.356	1.01±0.75
0.391	1.12±0.52
0.429	1.52±0.78
0.465	1.95±0.67
0.500	1.43±0.66
0.534	0.56±0.59
0.570	1.89±0.73
0.609	2.12±0.93
0.645	1.07±0.75

TABLE V. Relative differential transition probabilities of $4sd \rightarrow 1s$ two-photon decay in xenon in units of 10^{-9} keV^{-1} sr^{-2} at $\theta = 180°$. $E_0 = 34.498$ keV.

$x = E/E_0$	$\frac{1}{W_K}\frac{d^3W}{dE\, d\Omega_1 d\Omega_2}$
0.352	1.38±0.42
0.394	1.21±0.43
0.432	2.63±0.91
0.466	1.26±0.47
0.500	1.33±0.51
0.533	2.17±0.56
0.568	2.16±0.80
0.605	1.86±0.48
0.647	2.17±0.52

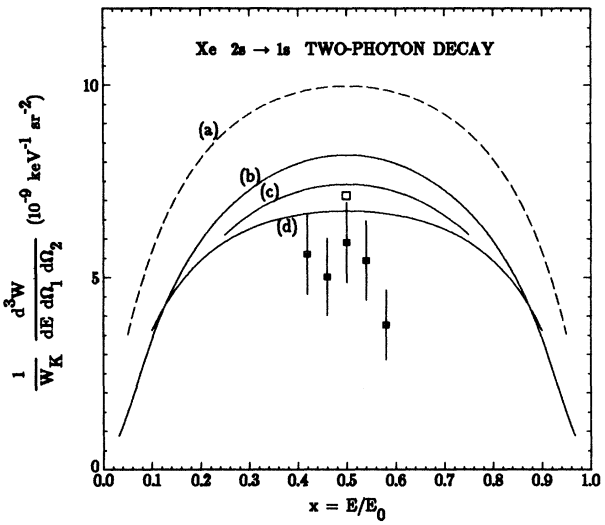

FIG. 8. Relative differential transition probabilities of $2s \rightarrow 1s$ two-photon decay in xenon atoms at 180°. Experimental results are shown by solid squares. Results derived from the theories of Shapiro and Breit [3] and Tung, Ye, Salamo, and Chan [7] for hydrogenic Xe ions are shown by the dashed curve (a). Results of calculations for Xe atoms with a K-shell vacancy are shown by the solid curves (b)–(d) and by the open square. They are the results of (b) a nonrelativistic calculation of Wu and Li [23], (c) a relativistic calculation of Mu and Crasemann [20,21], and (d) our calculation based on the theory of Bannett and Freund [19]; the open square at $x = 0.5$ is the result of a relativistic calculation of Tong, Li, Kissel, and Pratt [24].

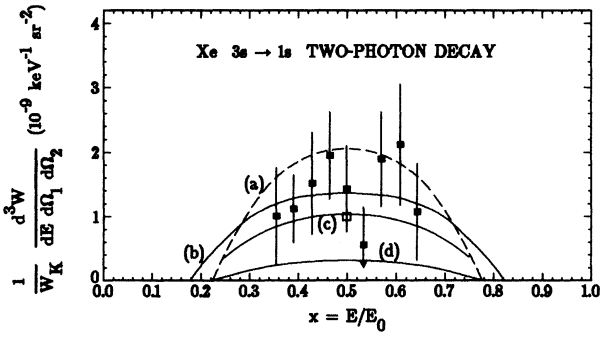

FIG. 9. Relative differential transition probabilities of $3s \rightarrow 1s$ two-photon decay in xenon at 180°. Experimental results are shown by solid squares. Values derived from the results of nonrelativistic calculations of Tung, Ye, Salamo, and Chan [7] and Florescu [8] for hydrogenic Xe ions are shown by the dashed curve (a). Results of calculations for Xe atoms with a K-shell vacancy are shown by the solid curves (b)–(d) and by the open square. They are the results of (b) a nonrelativistic calculation of Wu and Li [23], (c) a relativistic calculation of Mu and Crasemann [20,21], and (d) our calculation based on the theory of Bannett and Freund [18]; the open square at $x = 0.5$ is the result of a relativistic calculation of Tong, Li, Kissel, and Pratt [24].

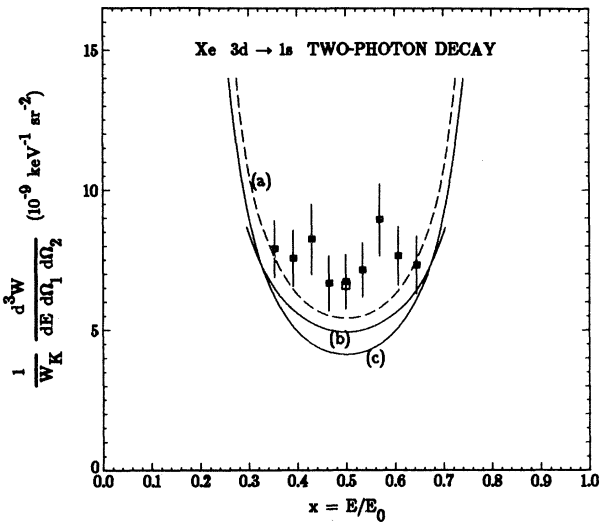

FIG. 10. Relative differential transition probabilities of $3d \rightarrow 1s$ two-photon decay in xenon at 180°. Experimental results are shown by solid squares. Values derived from the results of nonrelativistic calculations of Tung, Ye, Salamo, and Chan [7] and Florescu [8] for hydrogenic Xe ions are shown by the dashed curve (a). Results of calculations for Xe atoms with a K-shell vacancy are shown by the solid curves (b) and (c), and by the open square. They are the results of (b) a nonrelativistic calculation of Wu and Li [23] and (c) a relativistic calculation of Mu and Crasemann [20,21]; the open square at $x = 0.5$ is the result of a relativistic calculation of Tong, Li, Kissel, and Pratt [24].

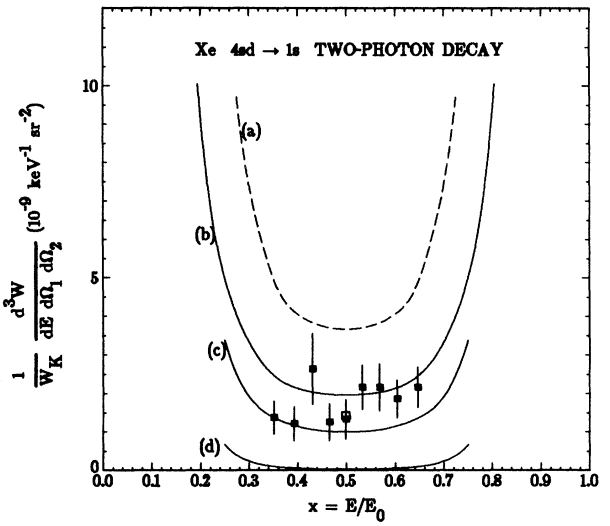

FIG. 11. Relative differential transition probabilities of $4sd \rightarrow 1s$ two-photon decay in xenon at 180°. Experimental results are shown by solid squares. Values derived from the results of nonrelativistic calculations of Tung, Ye, Salamo, and Chan [7] for hydrogenic Xe ions are shown by the dashed curve (a). Results of calculations for Xe atoms with a K-shell vacancy are shown by the solid curves (b)–(d) and by the open square. They are the results of (b) a nonrelativistic calculation of Wu and Li [23[, (c) a relativistic calculation of Mu and Crasemann [20,21], and (d) our calculation based on the theory of Bannett and Freund [18], multiplied by a factor of 10; the open square at $x = 0.5$ is the result of a relativistic calculation of Tong *et al.* [24].

TABLE VI. Average values of the theoretical and experimental relative differential transition probabilities of two-photon decay in xenon for the central 6-keV-wide intervals of photon energy and emission in the opposite directions. Abbreviations:; NR, nonrelativistic; *R*, relativistic; EDA, electric dipole approximation; RWF, Roothaan wave functions; FO, frozen orbitals; SCF, self-consistent field; Xe $\overline{K}$, *K*-shell vacancy state in xenon atom.

Two-photon decay	$2s \rightarrow 1s$	$3s \rightarrow 1s$	$3d \rightarrow 1s$	$4sd \rightarrow 1s$
Xe^{53+}, NR EDA, Ref. [3][a]	9.91			
Xe^{53+}, NR EDA, Ref. [7][a,b]	9.99	2.06	5.44	3.72
Xe^{53+}, NR EDA, Ref. [8][a]		2.01	5.59[c]	
Xe^{53+}, *R*, Ref. [24][b]	9.15	1.64	24.86	14.63
Xe $\overline{K}$, NR, RWF FO, Ref. [18][d]	6.68	0.31		0.004[e]
Xe $\overline{K}$, NR, SCF DA, Ref. [23][b]	8.26	1.39	8.42	1.97
Xe $\overline{K}$, *R*, SCR, Refs. [20,21]	7.36	0.97	4.85	1.12
Xe $\overline{K}$, *R*, SCF, Ref. [24][d]	7.13	1.00	6.60	1.42
Experimental results	5.06±0.45	1.40±0.30	7.34±0.47	1.66±0.27

[a]Values we derived from the results in the quoted reference.
[b]Value at $x = 0.5$ (not averaged value).
[c]The factor of 5 has not been used since a hydrogenic Xe ion is considered.
[d]Results of our calculation based on the theory in the quoted reference.
[e]Only $4s \rightarrow 1s$ two-photon decay is included.

Our value of the average relative differential transition probability of $2s \rightarrow 1s$ two-photon decay seems to be at variance with the theoretical results. We consider the difference to be real, at least partially. A systematic error of our results is possible due to the uncertainty of calibration of the absolute efficiency of the detectors, but it could change the results at most by 10%, while the most reliable theoretical results are 45% [21] and 41% [24] larger. The corresponding results for $3s \rightarrow 1s$ two-photon decay seem to be in reasonable agreement, while for $3d \rightarrow 1s$ and $4sd \rightarrow 1s$ two-photon decay the results of Tong, Li, Kissel, and Pratt [24] seem to agree well, but not the results of Mu and Crasemann [21]. A correction of the experimental results for the efficiency of the detectors would require multiplying all quoted experimental results on two-photon decay by the same factor.

ACKNOWLEDGMENTS

The authors wish to express their gratitude to Professor B. Crasemann and Dr. X. Mu for several discussions and exchange of results, and to Professor R. H. Pratt for discussions and for sending results prior to publication. Many thanks are due to Mr. S. Vidić and Mr. K. Kovačević for the help with the detectors, and to Dr. N. Bogunović, Dr. N. Gamberger, and Dr. Z. Marić of the Electronics Group of the R. Bošković Institute for the help with electronics and the transfer of data. This work was in part financially supported by the Ministry of Science, Technology, and Informatics of the Republic of Croatia, by the Federal Scientific Council of Yugoslavia, and by the U.S. National Science Foundation (Project No. PN-734).

[1] M. Göppert-Mayer, Ann. Phys. (Leipzig) **9**, 273 (1931).
[2] G. Breit and E. Teller, Astrophys. J. **91**, 215 (1940); L. Spitzer and J. L. Greenstein, *ibid.* **114**, 407 (1951).
[3] J. Shapiro and G. Breit, Phys. Rev. **113**, 179 (1959).
[4] B. A. Zon and L.P. Rapoport, Pis'ma Zh. Eksp. Teor. Fiz. **7**, 70 (1968) [JETP Lett. **7**, 52 (1968)].
[5] S. Klarsfeld, Phys. Lett. **30A**, 382 (1969).
[6] Particle Data Group, J. J. Hernández *et al.*, Phys. Lett. B **239**, 1 (1990).
[7] H. Tung, X. M. Ye, G. J. Salamo, and F. T. Chan, Phys. Rev. A **30**, 1175 (1984).
[8] V. Florescu, Phys. Rev. A **30**, 2441 (1984).
[9] A. Costescu, I. Brândus, and N. Mezinescu, J. Phys. B **18**, L11 (1985).
[10] S. P. Goldman and G. W. F. Drake, Phys. Rev. A **24**, 183 (1981).
[11] F. A. Parpia and W. R. Johnson, Phys. Rev. A **26**, 1142 (1982).
[12] R. C. Elton, L. J. Palumbo, and H. R. Griem, Phys. Rev. Lett. **20**, 783 (1968).
[13] E. A. Hinds, J. E. Glendenin, and R. Novick, Phys. Rev. A **17**, 670 (1978).
[14] H. Gould and R. Marrus, Phys. Rev. A **28**, 2001 (1983).
[15] P. H. Mokler, Th. Stöhlker, Ch. Kozhuharov, J. Ullrich S. Reusch, Z. Stachura, A. Warczak, A. Müller, R. Schuch, E. A. Livingston, M. Schulz, Y. Awaya, and T. Kambara, in *X-Ray and Inner-Shell Processes,* edited by T. A. Carlson, M. O. Krause, and S. T. Manson (American Institute of Physics, New York, 1990), p. 335.
[16] R. Marrus, V. S. Vicente, P. Charles, J. P. Briand, F. Bosch, D. Liesen, and I. Varga, Phys. Rev. Lett. **56**, 1683 (1986).
[17] I. Freund, Phys. Rev. A **7**, 1849 (1973).
[18] Y. Bannett and I. Freund, Phys. Rev. Lett. **49**, 539 (1982); Phys. Rev. A **30**, 299 (1984).
[19] K. Ilakovac, J. Tudorić-Ghemo, B. Bušić, and V. Horvat, Phys. Rev. Lett. **56**, 2469 (1986).
[20] X. Mu and B. Crasemann, Phys. Rev. Lett. **57**, 3039 (1986).
[21] X. Mu and B. Crasemann, Phys. Rev. A **38**, 4585 (1988).

[22] D. S. Guo, Phys. Rev. A **36**, 4267 (1987).
[23] Y.-J. Wu and J.-M. Li, J. Phys. B **21**, 1509 (1988).
[24] X.-M. Tong, J.-M. Li, L. Kissel, and R. H. Pratt, Phys. Rev. A **42**, 1442 (1990).
[25] K. Ilakovac, J. Tudorić-Ghemo, V. Horvat, N. Ilakovac, S. Kaučić, and M. Vesković, Nucl. Instrum. Methods A **245**, 467 (1986).
[26] S. I. Salem, S. L. Panossian, and R. A. Krause, At. Data Nucl. Data Tables **14**, 91 (1974).
[27] P. R. Bevington, *Data Reduction and Error Analysis for the Physical Sciences* (McGraw-Hill, New York, 1969).
[28] W. H. McMaster, N. K. Del Grande, I. H. Mallett, and J. H. Hubbell, Lawrence Livermore Radiation Laboratory Report No. UCRL-50174, Sec. II, Rev. 1, 1969 (unpublished).
[29] K. Ilakovac, V. Horvat, and N. Ilakovac, Nucl. Instrum. Methods **228**, 210 (1984).